# INSTALLATION AND TEST OF THE PHASE DRIFT MONITOR AT J-PARC LINAC

E. Cicek*, Z. Fang, Y. Fukui, K. Futatsukawa, S. Mizobata, KEK, Ibaraki, Japan
Y. Sato, Nippon Advanced Technology Co., Ltd., Tokai, Japan

*Abstract*

Achieving a stable RF field for all cavities in the J-PARC linac is one of the significant tasks for the successful operation of J-PARC. In particular, a long-term stable RF field is a crucial challenge in suppressing the drift of the injection beam momentum from the linac to the rapid cycling synchrotron (RCS). In addition, we found that environmental factors such as humidity and temperature cause RF phase drift in the cavities, resulting in the drift in the beam injection momentum, making the compensation of phase drift a priority job. To this end, a phase drift correction algorithm is carried out within the low-level radio frequency (LLRF) system at linac. Although this system has been operated successfully, we aim for an updated design to directly measure and correct the phase drift of the cavities operating at different frequencies. Therefore, a real-time phase drift compensation system based on a direct sampling technique deploying RF system-on-chip (RFSoC) technology is adopted to measure two different RF frequencies without local oscillator (LO) signals. This study presents the installation stage of the device in the linac and long-term cavity RF phase results.

## INTRODUCTION

The Japan Proton Accelerator Research Complex (J-PARC) linac consists of a negative hydrogen $H^-$ ion source (IS), 3 MeV radio frequency quadrupole (RFQ), 50 MeV drift-tube linac (DTL), 190.8 MeV separated-type DTL (SDTL), and 400 MeV annular ring coupled structure ACS, as shown in Fig. 1. The linac also has a medium-energy beam transport line 2 (MEBT2), which is equipped with two buncher cavities (B1 and B2), and L3BT (linac-to-3-GeV RCS beam transport). A 50 mA $H^-$ beam is injected into the rapid cycling synchrotron (RCS) through the L3BT line [1, 2].

The drift in the momentum of the injection beam must be within $\pm 0.05\%$ due to the RCS acceptance to avoid beam losses [3]. Environmental factors that can cause drift in beam injection momentum from the linac to the RCS are predominantly the humidity and temperature at the klystron gallery. Thus, stabilizing the accelerating RF field in the short-term and long-term is necessary during beam operation. A low-level radio frequency (LLRF) system with digital feedback (DFB) and feedforward (DFF) is utilized to fulfill the required specifications of $\Delta A/A < \pm 1\%$ peak-to-peak (pp) in amplitude and $\Delta\theta < \pm 1$ deg (pp) in phase [4]. Meanwhile, a compensation system using cavity phase monitors (henceforth referred to as "CPM") located at each RF station compensates for phase and amplitude drifts in RF frequencies of 324 MHz and 972 MHz individually [5].

Table 1: The Comparison of the Extant and Updated Phase Drift Compensation System

| Parameters | Extant | Updated |
|---|---|---|
| Device | Cavity phase monitor | Phase drift monitor |
| Technique | Downconverter + IF sampling | Direct sampling |
| LO | Used | Not used |
| Frequency | 324 MHz[a] or 972 MHz[a] | 324 MHz and 972 MHz |
| Key point | Conventional | RFSoC |

[a] Two frequencies are individually measured at CPMs.

Although the extant drift compensation system has proven reliable, measuring and correcting drift in RF cavities operating at different frequencies necessitates an updated technique. Therefore, we have developed a new system using a phase drift monitor (henceforth called "PDM") based on the Xilinx Zynq UltraScale+ RF system-on-chip (RFSoC) ZCU111 evaluation platform [6]. The comparison of extant and updated systems is listed in Table 1. Local oscillator (LO) signals, which may be a source of drift, are eliminated with the direct sampling technique where pick-up RF signals from accelerating cavities operating at 324 MHz and 972 MHz are directly digitized by analog-to-digital converters (ADC). The PDM calculates phase differences between cavities and compensates for drift in RF signals within dedicated DFB systems. This study presents the performance analysis completion of the PDM, its installation procedure, and long-term cavity RF phase measurement results.

## HARDWARE

The PDM architecture consists of a ZCU111 board, and the analog front end was implemented by the Mitsubishi Electric TOKKI Systems [7]. Figure 2 shows the hardware inside the PDM chassis and its front panel. The board was populated with Zynq UltraScale+ XCZU28DR-2FFVG1517 RFSoC combining a processing system and programmable logic in the same device. The processor runs Linux OS and integrates the experimental physics and industrial control system (EPICS) input/output controller (IOC) for data communication. The ZCU111 board contains eight 12-bit 4 GSPS RF-ADC channels (ADC00~07) and eight 14-bit 6.554 GSPS digital-to-analog (RF-DAC) channels (DAC00~07). An ethernet interface allows integration with the linac control system. An RFMC connector on the board

* ecicek@post.kek.jp

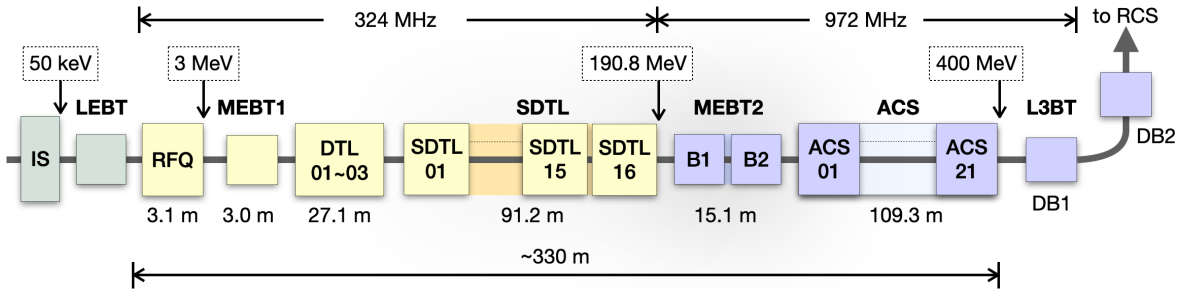


Figure 1: J-PARC linac configuration.

provides direct access to the RFSoC analog inputs. The analog front-end comprises an RF differential breakout card (AES-LPA-502-G) [8] and ADC wideband panel mount balun boards (ADC-WB-BB) [9]. The baluns are employed to convert RF signals into differential outputs and provide access between eight analog input channels from the front panel to the breakout card. The breakout card is directly connected to the RFMC mezzanine interface.

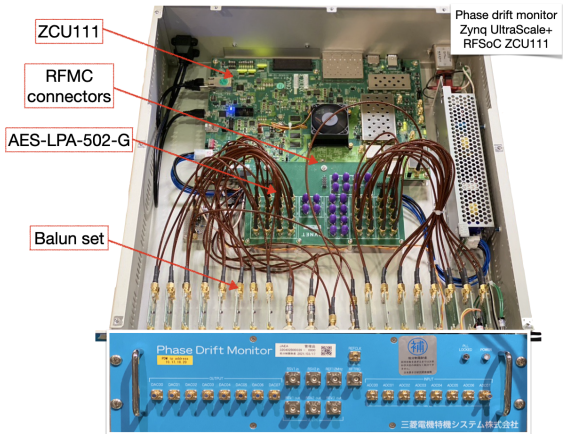


Figure 2: (Color online) The top view (top) and front view (bottom) of the PDM chassis.

## PERFORMANCE ANALYSIS COMPLETION

The first results regarding performance analysis of the PDM were reported in [10]. Afterward, to evaluate the drift in phase differences measured on ADC channels, PDM was placed in a commercial environmental test chamber (ESPEC PDR-3J) [11], as illustrated in Fig. 3.

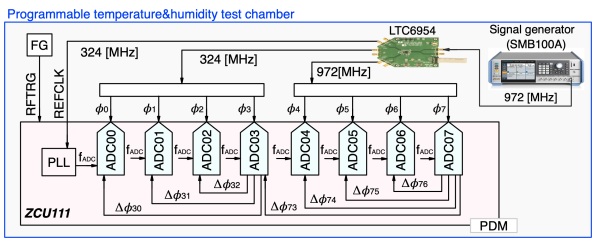


Figure 3: Test bench of the temperature and humidity characteristics measurement for the PDM.

Figure 4 shows the temperature and humidity characteristics of the PDM. Input channels from ADC00 to ADC03 and ADC04 to ADC07 measured phase of 324 MHz (from $\phi_0$ to $\phi_3$) and 972 MHz (from $\phi_4$ to $\phi_7$) RF signals, respectively. $\phi_3$ and $\phi_7$ were assigned as reference phases for two different frequencies, and phase differences with respect to the references were computed. The temperature inside the chamber ($T_{set}$) was changed from 23°$C$ to 31°$C$ (round trip) with a 2°$C$/3 h ramping rate at a fixed humidity of 65%RH. Afterward, humidity ($RH_{set}$) was changed from 15%RH to 65%RH (round trip) with a ramping rate of 25%RH/24 h steps at a fixed temperature of 27°$C$.

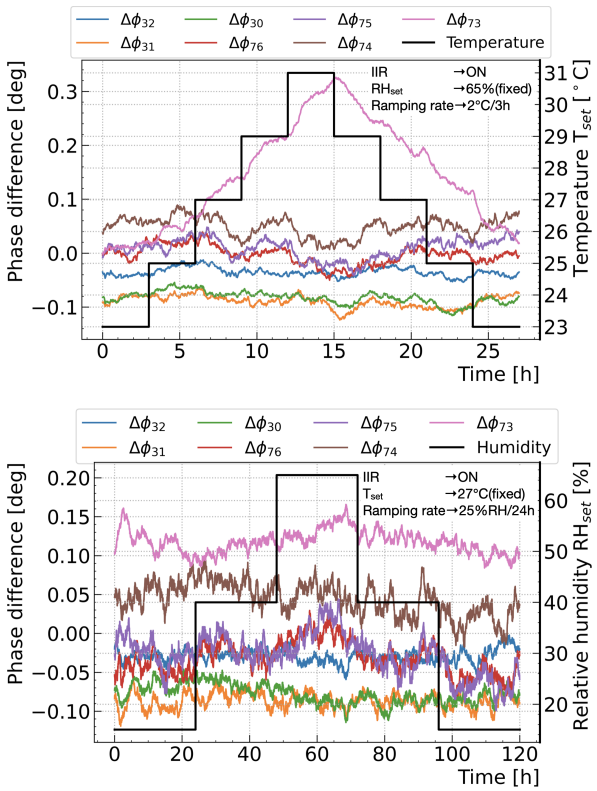


Figure 4: Temperature (top) and humidity (bottom) dependence of RF phase differences. $\Delta\phi_{32}$, $\Delta\phi_{31}$, and $\Delta\phi_{30}$ denote phase differences between ADC03 and ADC02, ADC03 and ADC01, and ADC03 and ADC00, respectively. $\Delta\phi_{76}$, $\Delta\phi_{75}$, and $\Delta\phi_{74}$ are phase differences between ADC07 and ADC06, ADC07 and ADC05, and ADC07 and ADC04, respectively.$\Delta\phi_{73}$ is phase difference between references.

The temperature and humidity characteristics results of the PDM using an infinite impulse response (IIR) filter, the simplest LPF, implementation are listed in Table 2. Drift in phase differences (pp) of 324 MHz ($\Delta\varphi_{324}$) and 972 MHz ($\Delta\varphi_{972}$) ADC channels per 1°$C$ and 1%RH steps were very small. Though the relative phase difference ($\Delta\phi_{73}$ ) had a similar trend with rising and decreasing temperature and humidity, the drift denoted as $\Delta\varphi_{ref}$ was also measured as small. In addition, the PDM was less humidity-dependent.

Table 2: Summary of Temperature and Humidity Characteristics for the PDM

| **Ramping rate** | **Step** | **Phase drift [deg]** | | |
|---|---|---|---|---|
| | | $\Delta\varphi_{324}$ | $\Delta\varphi_{972}$ | $\Delta\varphi_{ref}$ |
| 2°$C$/3 h (fixed 65%RH) | 1°$C$ | 1.23E-3 | 6.68E-3 | 3.75E-2 |
| 25%RH/24 h (fixed 27°$C$) | 1%RH | 1.20E-4 | 6.63E-4 | 4.20E-4 |

Meanwhile, long-term temperature and humidity in the MEBT2B1 LLRF rack, where the PDM was installed, can be kept within 1°$C$ (pp) and 1%RH (pp), respectively. Accordingly, the PDM is ideal to be implemented in the LLRF system in terms of temperature and humidity characteristics.

## INSTALLATION

Figure 5 shows the PDM installed at the MEBT2B1 LLRF control rack, where a constant temperature and humidity environment is provided. The cavity pick-up RF signals from SDTL15A and SDTL15B, SDTL16A, and SDTL16B tanks operating at 324 MHz were connected to the channels of ADC00, ADC01, ADC02, and ADC03 channels, respectively. In addition, the pick-up signals from 972 MHz MEBT2B1, MEBT2B2, and ACS1 cavities were connected to ADC04, ADC05, and ADC06, channels, respectively.

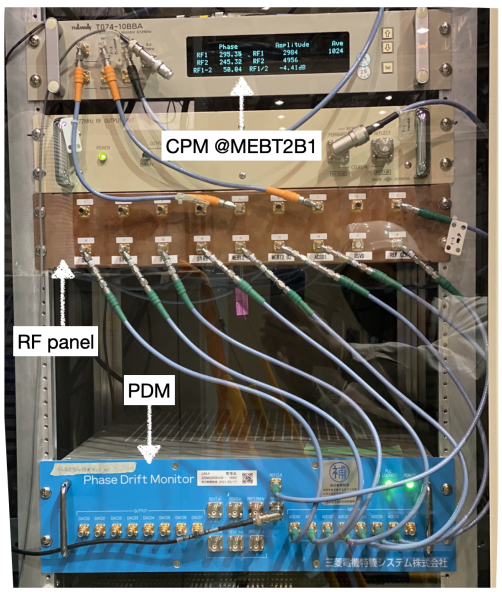


Figure 5: Photograph of PDM installed at MEBT2B1 station.

To connect cavity pick-up loop and reference clock (REFCLK) signals to MEBT2B1 control rack, 3/8-inch foam dielectric, phase-stabilized Andrew Heliax coaxial cables were used. Front panel mount SMA cables were used to connect the eight analog input channels to an RF panel in the control rack. RF power for 324 MHz REFCLK generated from an RF&CLK board in the SDTL16 RF station was +3.8 dBm. RF trigger (RFTRG) signal was provided from the timing system at the SDTL16 RF station.

## LONG-TERM PHASE DIFFERENCES

The PDM was tested online to evaluate long-term cavity RF phase differences because we aimed to utilize it within the LLRF system. Figure 6 shows the RF phase measurement scheme. Cavity phases of $\phi_{23\_vs}$, the vector sum (VS) phase of SDTL16A and SDTL16B tanks, and $\phi_{4\_pdm}$ were assigned as reference phases because the MEBT2B1 and SDTL16 19-inch LLRF control racks were placed in a constant local temperature&humidity environment. $\phi_{01\_vs}$ is the VS RF phase of SDTL15A and SDTL15B tanks.

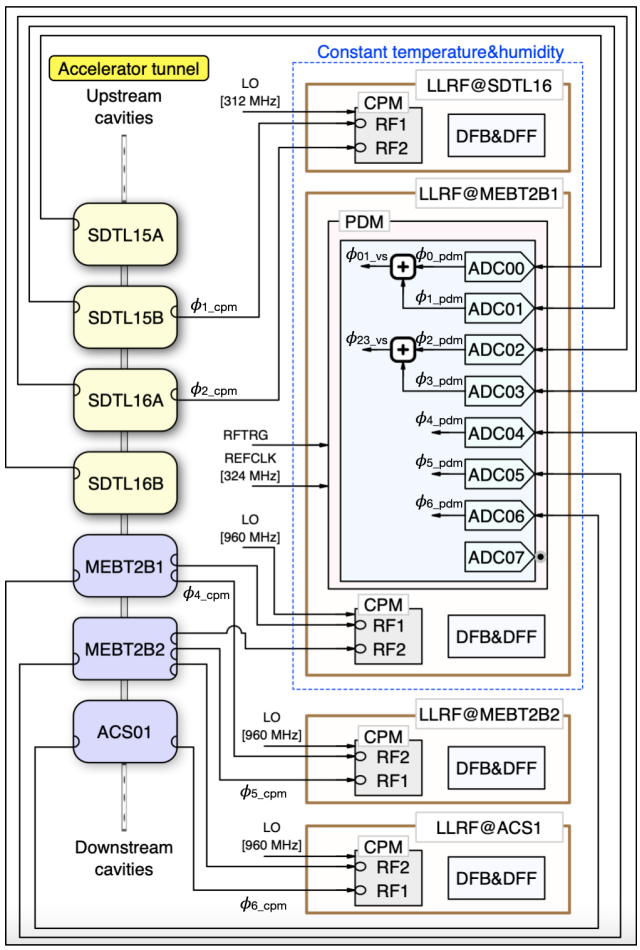


Figure 6: Long-term cavity RF phase measurement scheme on the PDM and CPMs. RF1 and RF2 inputs on the CPMs represent ADC inputs where two neighbor cavity tanks are connected. The phases from $\phi_{0\_pdm}$ to $\phi_{6\_pdm}$ denote the RF phases of each cavity tank measured by the PDM.

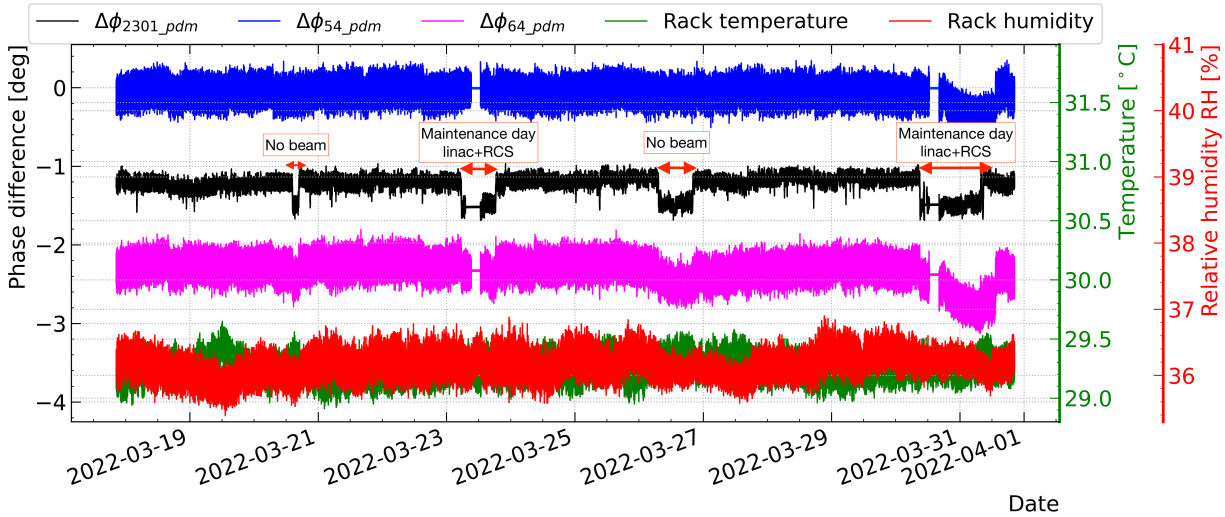


Figure 7: Long-term cavity RF phase differences, measured and computed in the PDM when there is no change in the MEBT2B1 rack temperature and humidity. $\Delta\phi_{2301\_pdm}$ represents VS phase difference between SDTL16 and SDTL15; $\Delta\phi_{54\_pdm}$ denotes phase difference between MEBT2B2 and MEBT2B1; and $\Delta\phi_{64\_pdm}$ represents phase difference between ACS01 and MEBT2B2 cavities.

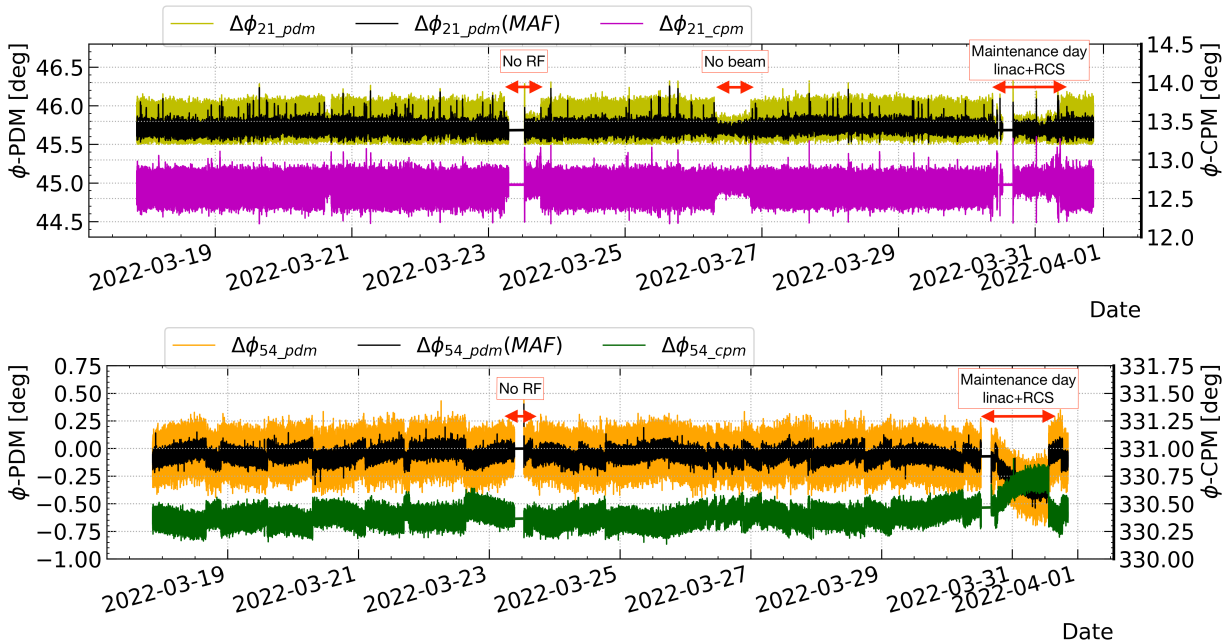


Figure 8: Comparison of long-term cavity RF phase differences measured and computed on the PDM and CPMs: (top) $\Delta\phi_{21\_pdm}$ and $\Delta\phi_{21\_cpm}$ represent the phase differences between SDTL16A and SDTL15B tanks, (bottom) $\Delta\phi_{54\_pdm}$ and $\Delta\phi_{54\_cpm}$ denote the phase differences between MEBT2B2 and MEBT2B1 cavities. The black plots depict the phase difference measured on the PDM with a MAF. MAF represents a moving average filter.

Figure 7 presents the long-term RF phase differences with respect to reference phases that can be measured only on the PDM. Figure 8 shows phase differences compared with permanently installed and successfully operated CPMs. Hereby, the EPICS archiver appliance stored real-time cavity RF phase data as well as temperature and humidity data inside the MET2B1 rack. The results measured on the PDM were consistent with those on the CPMs; no change in the center of phase differences for two weeks where stable temperature and humidity in the rack were provided, see Fig. 8.

As the last and primary step, we evaluated $\Delta\phi_{rel}$ relative phase difference derived from the phase difference between two different frequencies of 324 MHz and 972 MHz on the PDM. Write down an expression of the relative phase difference,

$$\Delta\phi_{rel} = \Delta\phi_{23\_vs} - (\Delta\phi_{4\_pdm}/3), \qquad (1)$$

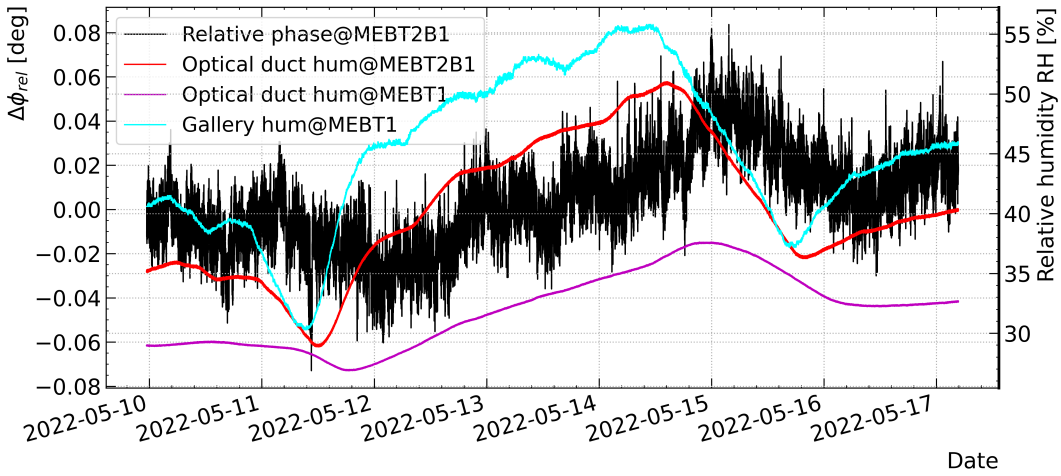


Figure 9: Humidity dependency of the relative phase difference.

where $\Delta\phi_{23\_vs}$ and $\Delta\phi_{4\_pdm}$ denote phase changes (pp) in the reference channels of ADC03 (SDTL16 VS) and ADC04 (MEBT2B1), respectively. Figure 9 presents the humidity dependence of relative phase difference evaluated for about one week. The relative phase difference tends to be similar to the humidity change in the klystron gallery and the optical duct, where RF reference signals are distributed [12].

## CONCLUSIONS

Phase differences between 324 MHz cavities and their respective reference phase, as well as that of 972 MHz cavities, are measured to be stable for the long-term on the CPMs and PDM. However, we have found that environmental factors, particularly humidity changes, cause long-term phase drift in the relative phase difference, critical information for stabilizing accelerating RF fields through linac cavities operating at two different frequencies. The source of variation in the relative phase difference is thought to be humidity change in the optical duct or klystron gallery. To this end, the PDM will be employed within the LLRF system to compensate for possible phase and amplitude drifts in cavity RF signals by eliminating environmental effects, which is crucial for a stable long-term operation.

## ACKNOWLEDGMENTS

Special thanks to the Mitsubishi Electric Tokki Systems Corporation team for implementing a phase drift monitor. The authors would also like to thank the Mitsubishi SC members for their excellent work during the device installation.

## REFERENCES

[1] I. Masanori, "Beam commissioning and operation of the J-PARC linac", *Prog. Theor. Exp. Phys.*, vol. 2012, no. 1, p. 02B002, 2012. doi:10.1093/ptep/pts019

[2] H. Ao *et al.*, "First annular-ring coupled structure cavity for the Japan Proton Accelerator Research Complex linac", *Phys. Rev. ST Accel. Beams*, vol. 15, p. 051005, 2012. doi:10.1103/PhysRevSTAB.15.051005

[3] K. Moriya, H. Harada, Y. Liu, and M. Otani, "Energy measurement and correction for stable operation in J-PARC", *J. Phys. Conf. Ser.*, vol. 1350, p. 012140, Sep. 2019. doi:10.1088/1742-6596/1350/1/012140

[4] Z. Fang *et al.*, "Auto-tuning systems for J-PARC LINAC RF cavities", *Nucl. Instrum. Methods Phys. Res. A.*, vol. 767, p. 135, 2014. doi:10.1016/j.nima.2014.08.014

[5] K. Futatsukawa *et al.*, "Performance of Cavity Phase Monitor at J-PARC Linac", *in Proc. 4th International Particle Accelerator Conf. (IPAC'13)*, Shanghai, China, 12-17 May 20173 paper WEPFI017, pp. 2738-2740.

[6] AMD Xilinx, Zynq UltraScale+ RFSoC ZCU111 Evaluation Kit, https://www.xilinx.com/products/boards-and-kits/zcu111.html

[7] Mitsubishi Electric TOKKI Systems Corporation, http://www.melos.co.jp/english/products/

[8] AES-LPA-502-G, RF Breakout Card for Zynq UltraScale+ RFSoC, https://www.avnet.com/shop/emea/products/avnet-engineering-services/aes-lpa-502-g-3074457345642032518/

[9] ADC wideband balun board, https://www.ti.com/tool/ADC-WB-BB

[10] E. Cicek *et al.*, "A Recent Upgrade on Phase Drift Compensation System for a Stable Beam Injection at J-PARC Linac", *in Proc. 12th International Particle Accelerator Conf. (IPAC'21)*, Campinas, SP, Brazil, 24-28 May 2021 paper WEPAB297, pp. 3357–3359.

[11] ESPEC temperature&humidity chamber, https://www.espec.co.jp/english/products/

[12] K. Futatsukawa *et al.*, "Upgrade of the RF Reference Distribution System for 400 MeV LINAC at J-PARC", *in Proc. 3rd International Particle Accelerator Conf. (IPAC'12)*, New Orleans, Louisiana, USA, 20-25 May 2012 paper WEPPD050, pp. 2630–2632.